ACS Sustainable Chemistry & Engineering

Research Article

Cite This: ACS Sustainable Chem. Eng. 2018, 6, 12166−12175

pubs.acs.org/journal/ascecg

SbSI Nanocrystals: An Excellent Visible Light Photocatalyst with Efficient Generation of Singlet Oxygen

Chong Wang,[†,#] Mian Zhang,[‡,#] Yong Fang,[§] Gaoyu Chen,[∥] Qi Li,[†] Xuexi Sheng,[†] Xiangxing Xu,*[,†] Junfeng Hui,*[,∥] Yaqian Lan,[†] Min Fang,[†] Xiaojun Wang,[⊥] Xinping Wang,[§] Zhihui Dai,[†] Jianchun Bao,[†] and Peng Wang*[,‡]

[†]Jiangsu Key Laboratory of Biofunctional Materials, School of Chemistry and Materials Science, Nanjing Normal University, 1 Wenyuan Road, Nanjing 210046, P. R. China

[‡]National Laboratory of Solid State Microstructures, College of Engineering and Applied Sciences and Collaborative Innovation Center of Advanced Microstructures, Nanjing University, 22 Hankou Road, Nanjing 210093, P. R. China

[§]State Key Laboratory of Coordination Chemistry, School of Chemistry and Chemical Engineering, Collaborative Innovation Center of Advanced Microstructures, Nanjing University, 22 Hankou Road, Nanjing 210093, P. R. China

[∥]Shaanxi Key Laboratory of Degradable Biomedical Materials, Shaanxi R&D Center of Biomaterials and Fermentation Engineering, School of Chemical and Engineering, Northwest University, 229 Taibai North Road, Xi'an 710069, P. R. China

[⊥]College of Life Sciences, Nanjing Normal University, 1 Wenyuan Road, Nanjing 210046, P. R. China

Supporting Information

ABSTRACT: Antimony sulfoiodide (SbSI) is commonly known as a prototypical ferroelectric semiconductor. We report herein a top-down strategy of ball-milling followed by size selective centrifugation to prepare SbSI nanocrystals (NCs). Taking the well dispersed SbSI NCs of the average size of 80 nm as photocatalyst, a record high visible light efficiency in photodegradation of methyl orange (MO) in water was achieved. By using a 300 W xenon lamp with a 420 nm cutoff filter and with the SbSI NCs of 1 g/L, the MO solution of 30 mg/L can be degraded ∼99% in 10 s. The pseudo-first-order rate constant (k) of the photodegradation is k = 0.42 s^{-1}. For high concentrated MO of 150 mg/L, it can be ∼99% degraded in 30 s at an elevated temperature of 65 °C (k = 0.15 s^{-1}). With further increase of the SbSI NCs concentration to 4 g/L, the 150 mg/L MO can be ∼99% degraded in 1 min at room temperature (k = 0.095 s^{-1}). The small size of the SbSI NCs and efficient generation of singlet oxygen were found to be the key factors for the outstanding performance.

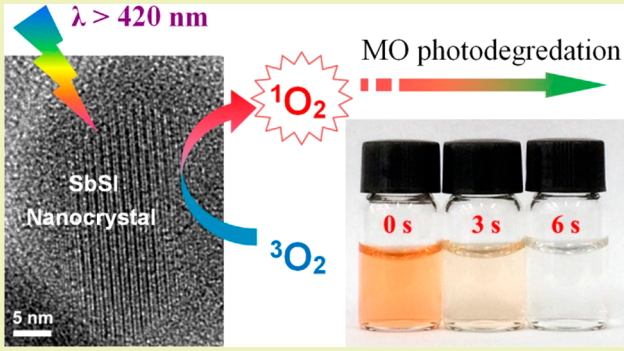

KEYWORDS: *SbSI, Nanocrystals, Photocatalysis, Photodegradation, Singlet oxygen, Visible light*

INTRODUCTION

Due to the pressure from the worldwide energy crisis and requirement of the environmental protection, photocatalysts have aroused intensive interest as a powerful solution since the initial work of Fujishima and Honda in 1972.[1−4] Among the various photocatalytic materials for cleanup of organic pollutants in water, the most widely investigated is titanium dioxide (TiO_2), which has a wide band gap of 3.2 eV that works effectively under ultraviolet irradiation.[5−9] Since the visible light composes ∼46% of the irradiation energy from the solar light, significantly above the ∼4% of the ultraviolet portion, continuous efforts have been devoted to searching for effective visible light active photocatalysts.[10−12] Typical visible light photocatalysts include the inorganic materials of doped TiO_2;[13−15] plasmonic nano-sized metals, e.g., Au, Ag, or Cu;[16,17] bismuth-based semiconductors, e.g., $BiVO_4$, Bi_2MoO_6, BiOX (X = Cl, Br, or I),[18−23] etc.; the organic polymeric graphitic carbon nitride (g-C_3N_4);[24,25] graphene quantum dots;[26] the supramolecular system, such as self-assembled perylene-3,4,9,10-tetracarboxylic diimide (PDINH);[27] hyper-cross-linked polynaphthalene nanoparticles (PNNs);[28] etc. Visible light photocatalysts with heterostructures, such as the TiO_2-, graphene-, or g-C_3N_4-based materials, were also demonstrated as having a better performance than that of each of the composed monophases, owning to the more effective charge separation.[29−33] Black phosphorus nanosheets were recently reported to be a effective ultraviolet−visible

Received: May 30, 2018
Revised: July 16, 2018
Published: July 30, 2018

DOI: 10.1021/acssuschemeng.8b02498
ACS Sustainable Chem. Eng. 2018, 6, 12166−12175

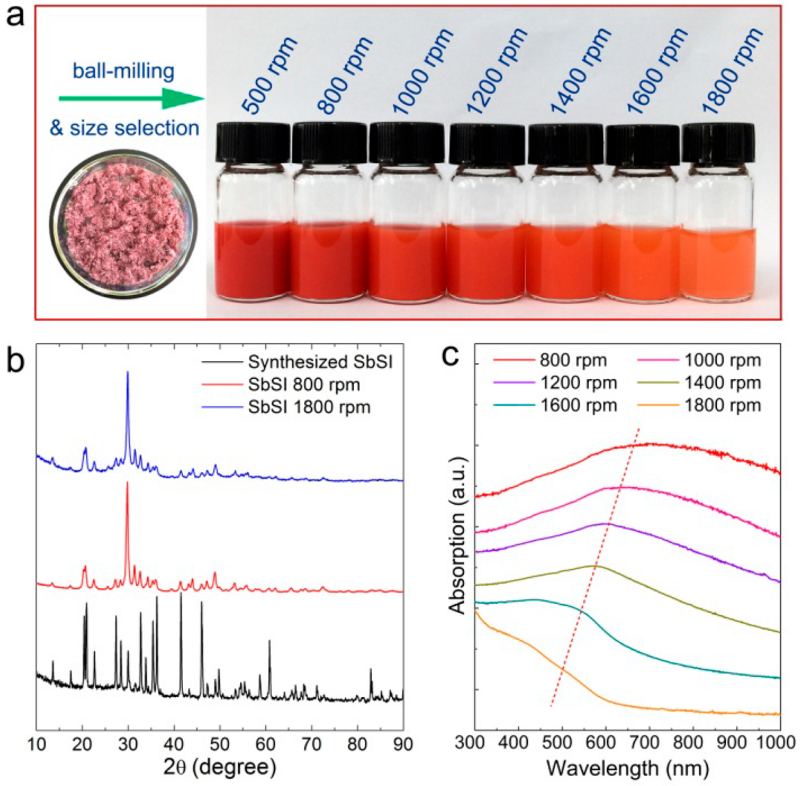

Figure 1. (a) Images of the hydrothermally synthesized SbSI crystals (left) and the fractions of SbSI redispersed in water after ball-milling and size selective centrifugation (right). (b) XRD patterns of the as synthesized SbSI crystals and size selected SbSI. (c) UV−vis absorption spectra of the size-selected SbSI colloidal solutions.

(UV−vis) light photosensitizers, due to their efficient generation of singlet oxygen.[34,35]

In developing a visible light photocatalyst, there are some general rules to follow. The first is the energy rule. The energy band of the photocatalyst should overlap with the visible light, either for exciton formation or plasmonic absorption. For a photocatalyst with a heterostructure, the energy structure needs to be rationally designed, e.g., to promote the separation of charges. Second, with the advances of nano science and techniques, the importance of combining the control of nano size and crystal structure to achieve enhanced photocatalytic activity is widely realized.[5−9] Last, due to the surface where charges and/or excitons interact with the reagent, surface engineering takes a critical role in improving photocatalytic performance.[36−39] In most cases, these rules interact with each other as a coupled system.

Guided by these rules, we focus the crosshair to the nano sized antimony sulfoiodide (SbSI). SbSI is chemically analogous to the photocatalysts BiOX (X = Cl, Br, or I) as a V−VI−VII compound. Historically, the SbSI crystal came into the sight of scientists in the 1960s, owing to the finding that it is photoconductive and has a ferroelectric phase transition near room temperature, exhibiting spontaneous electric polarization.[40−43] During the past two decades, micro- and nano-sized SbSI with tunable size and morphology were synthesized by bottom-up chemical methods. Its application potentials in gas sensing, thermal imaging, ferroelectric, piezoelectric, optoelectronic, and photovoltaic devices has been investigated and proposed.[44−49] SbSI has the merit of a suitable bandgap of ∼1.8 eV, along with being thermally stable, environmentally friendly, and having an abundance of raw resources; therefore, it is a promising candidate of visible light photocatalyst. Herein, we demonstrated a top-down strategy, ball-milling of bulk SbSI crystals followed by the size selective centrifugation, to prepare SbSI nanocrystals (NCs) exhibiting the quantum confinement effect. These SbSI NCs showed ultrahigh visible light photodegradation of dyes. By using a 300 W xenon lamp with a 420 nm cut-off filter and with the SbSI NCs (average size of 80 nm) of 1 g/L, the MO solution of 30 mg/L can be degraded to ∼99% in 10 s; for the MO concentration of 150 mg/L as the highest, an ∼99% degradation is achieved in 30 s at 65 °C. With further increase of the SbSI NCs concentration to 4 g/L, the 150 mg/L MO can be ∼99% degraded in 1 min at room temperature.

EXPERIMENTAL SECTION

Materials. Antimony chloride ($SbCl_3$, ≥ 99.0%), thiorea ($CS(NH_2)_2$, ≥ 99.0%), ammonium iodide (NH_4I, ≥ 99.0%), methyl orange (MO, Ind.), and ethanol (AR, ≥ 99.7%) were purchased from Sinopharm Chemical Reagent Co., Ltd. The TiO_2 NCs (P25: anatase 80%, rutile 20%) were from Degussa Co., Ltd.. All of the chemicals were used as received without further purification.

Synthesis. The SbSI NCs were prepared by a two-step process. First, bulk SbSI crystals were synthesized by a hydrothermal method. Typically, $SbCl_3$ (4 mmol), $(NH_2)_2CS$ (4 mmol), and 21.00 mmol NH_4I (20 mmol) were added to a stainless steel autoclave with a polytetrafluoroethylene liner, which contains 30 mL of HCl aqueous solution (1.0 M). The autoclave was then heated at 160 °C for 4 h. Then, the autoclave was cooled to room temperature naturally, the resulting precipitate was collected by filtration and washed with distilled water and ethanol. After being dried in an air oven at 80 °C, the needle-like crystalline SbSI with a deep red color was obtained. In the second step, a proper amount of the as-synthesized SbSI crystals was loaded for planetary ball-milling. The agate milling tanks are 100

DOI: 10.1021/acssuschemeng.8b02498
ACS Sustainable Chem. Eng. 2018, 6, 12166−12175

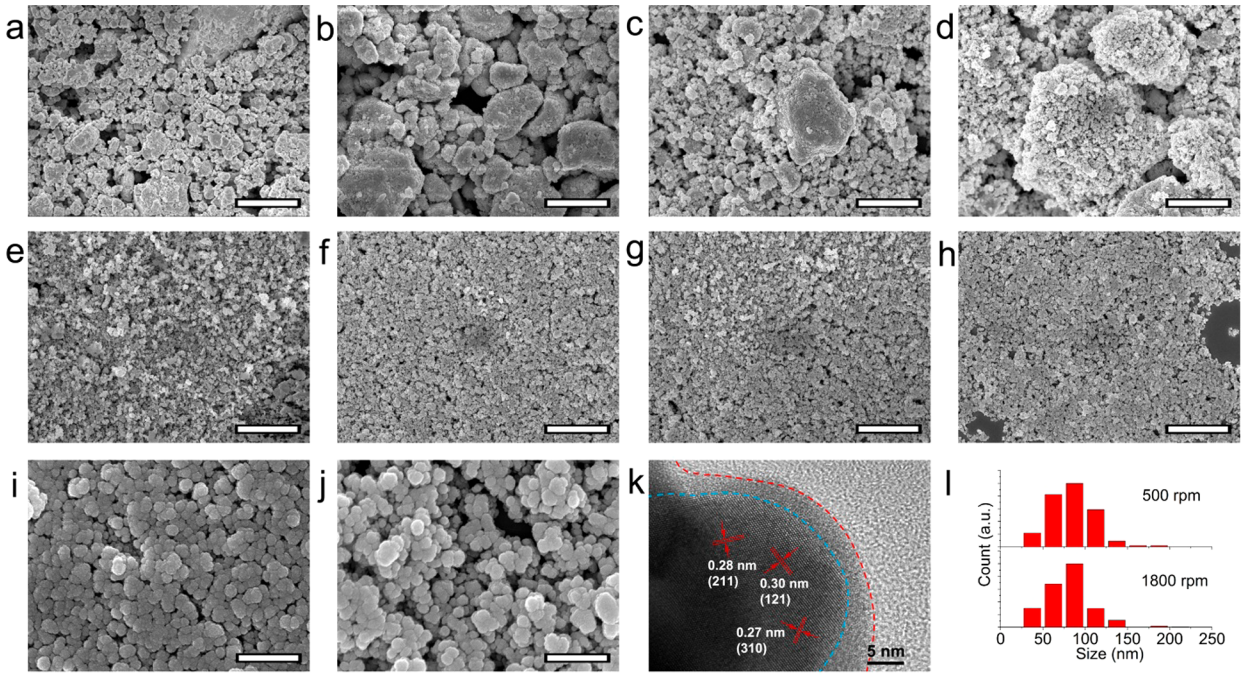

Figure 2. SEM images of the SbSI NCs fractions of (a) before size selection, (b) 500, (c) 800, (d) 1000, (e) 1200, (f) 1400, (g) 1600, (h) 1800, (i) 500, and (j) 1800 rpm. (k) HRTEM images of a SbSI NC of the 1800 rpm fraction, showing the crystalline core and an amorphous shell. (l) Size distribution of the primary SbSI NCs (scale bar: (a)−(h) 5 μm, (i) and (j) 500 nm).

mL each, with 2 mm and 5 mm agate balls in them. After milling for 5 h, red powder was obtained for further use.

Size Selective Centrifugation. The SbSI-milled powder was dispersed in water via ultrasonication to form a colloidal solution. This original solution was then centrifuged with proper speed (round per minute, rpm) and time (1 min in this work) to get precipitated SbSI samples. Following the first 500 rpm centrifugation, successive 800, 1000, 1200, 1400, 1600, and 1800 rpm centrifugations were carried out to get according fraction samples. These size-sorted SbSI nanocrystals were dried in an air oven at 60 °C for 8 h for further characterization and photocatalytic degradation experiments.

Method of Photocatalytic Degradation. Typically, 10−200 mg of SbSI powder was added to 50 mL of MO aqueous solution of 30 mg/L or 150 mg/L in a 100 mL beaker. Before illumination, the suspension was stirred in the dark environment for 20 min to establish the adsorption and desorption equilibrium between the dye and catalyst surface. A 300 W Xe lamp operating at the light power of ~400 mW/cm^2 equipped with a 420 nm filter was used to provide the visible light irradiation. The solution was kept stirring during the photodegradation. Samplings were taken at intervals followed by centrifugation to separate SbSI as deposition. The supernatant liquid was measured by UV−vis absorption analysis to determine the residual MO concentration.

Instruments. The power X-ray diffraction (XRD) patterns were recorded using a D/max 2500 VL/PC diffractometer equipped with graphite monochromatized Cu Kα radiation (λ = 0.15406 nm). The transmission electron microscopy (TEM) images were recorded on a JEM-200CX, with an accelerating voltage of 80 kV. The high-resolution transmission electron microscopy (HRTEM) images were taken on a JEOL-2100F, with an accelerating voltage of 200 kV. The scanning electron microscopy (SEM) images were measured by a JEOL JSM-7600F equipped with an energy dispersive spectroscopy (EDS). Nitrogen adsorption−desorption isotherms were measured at 77 K on a Quantachrome Instruments Autosorb AS-6B. Specific surface area was calculated by the Brunauer−Emmett−Teller (BET) method. The UV−vis spectra were measured on a spectrometer Cary 50. A 300 W Xe lamp (PLS-SXE300) equipped with a UV cut-off filter (λ > 420 nm) and a portable UV lamp (ZF-7A, 365 nm 8 W and 254 nm 8 W) were used as the light sources. The XPS spectrum was recorded by a PHI 5000 Versa Probe (U1VAC-PHI). The high angle annular dark field scanning transmission electron microscopy (HAADF-STEM) images and EDS elemental mappings were acquired using a FEI Titan^3 G2 60-300 microscope, operated at an accelerating voltage of 300 kV, equipped with double aberration correctors and Super-X EDS detectors. The photoelectrochemical (PEC) properties were measured on a Zahner PEC workstation (Zahner, Germany). The cyclic voltammetry (CV) curves were measured by a CHI 660D electrochemical workstation.

RESULTS AND DISCUSSION

Catalyst Characterizations. Figure 1a shows the size-selected SbSI particles redispersed in water. The XRD measurement shows that the synthesized needle-like SbSI is pure and has a orthorhombic phase structure, with the pattern consistent with the standard Joint Committee on Powder Diffraction Standards (JCPDS) Card no. 88-0988. The centrifugation fractions of the SbSI particles have the same XRD pattern (Figure 1b) but broadened peaks, indicating the crystal size down to the nanoscale. In aqueous solution, the color of the SbSI colloidals changes from deep red to orange for the 500−1800 rpm samples. Accordingly, the UV−vis absorption peak undergoes a blue shift from ~700 (1.77 eV) to ~500 nm (2.48 eV) (Figure 1c). The 500 rpm sample is not included because it undergoes rapid precipitation. The SEM measurement shows that the SbSI of the 500 rpm fraction contains SbSI particles with an average size of 1.7 μm (Figure 2b). Magnified SEM scan and TEM/HRTEM measurements indicate that those micron particles are aggregates of small primary SbSI NCs (Figures 2i,j and S1−S9). For each fraction, the average size of the primary SbSI NCs was almost unchanged, ~80 nm (Figure 2l). The size of the aggregates is monotonically decreased with higher centrifugation speeds from microns to <500 nm (Figure S8). Since the crystal structure is unchanged, the blue shift of the absorption is suggested to be caused by the quantum confinement effect. It

DOI: 10.1021/acssuschemeng.8b02498
ACS Sustainable Chem. Eng. 2018, 6, 12166−12175

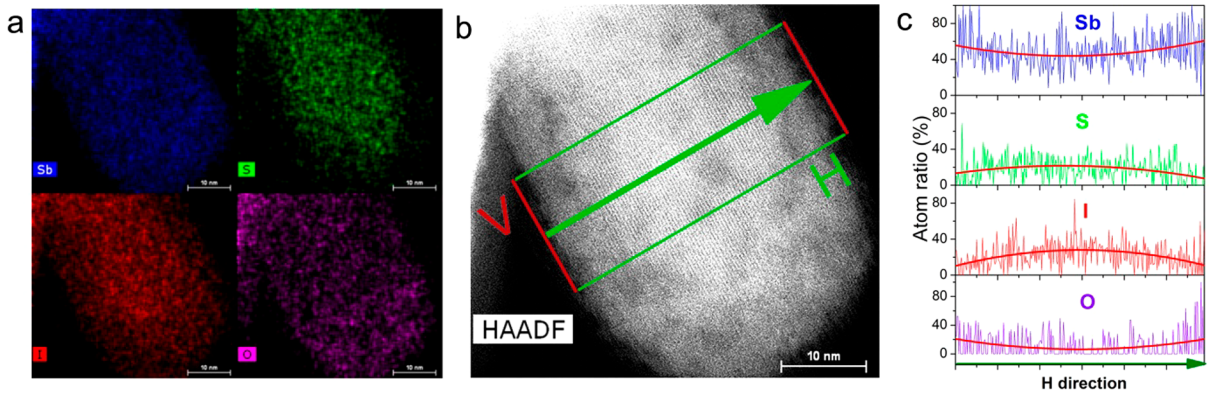

Figure 3. (a) The EDS mapping of the Sb, S, I, and O of a typical SbSI NC, (b) its HAADF-STEM image, and (c) the corresponding line scan of the element distribution.

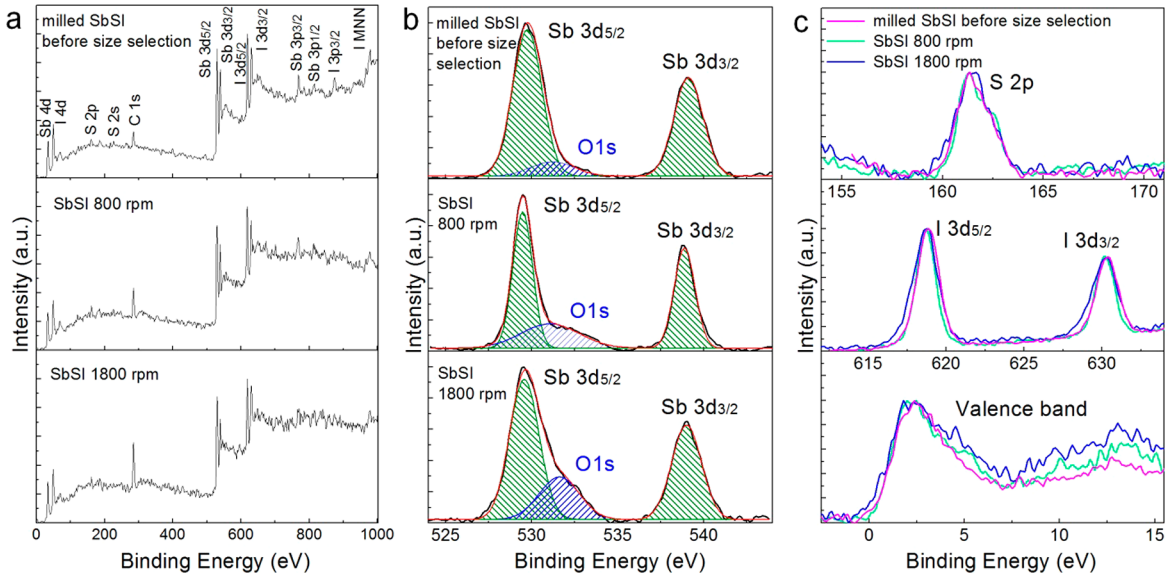

Figure 4. (a) The XPS survey spectrum; (b) Sb 3d and O 1s spectrum; and (c) S 2p, I 3d, and valence band spectrum of the SbSI samples.

is supported by the fact that SbSI has a huge dielectric constant around room temperature and therefore an enormous exciton Bohr radius of 1300 nm, much larger than that of the common QDs, such as CdSe, PbS, AgS_2, or InAs QDs, etc.[50] With this regard, both the size of the primary SbSI NCs and their aggregates contribute to the quantum confinement effect. SbSI is an indirect bandgap semiconductor,[51] and it is not surprising to find the samples nonfluorescent.

The HRTEM discovered that all of these SbSI NCs have an amorphous shell of 3−5 nm and a SbSI crystalline core (Figure 2k). This feature structure is ubiquitously observed in all of the SbSI fraction samples (Figure S9). The EDS mapping reveals that the SbSI NCs not only contain antimony (Sb), sulfur (S), and iodine (I) but also oxygen (O), shown in Figure 3. Figure 3c is the atom distribution of Sb, S, I, and O along the H direction; the percent ratio data at each point on the H-axis were obtained from the statistic summary along the line of the V-axis (red line in Figure 3b). The qualitative analysis depicts that the S and I percent ratio decreases from the inside to the shell, while the Sb and O percent ratio shows an increase trend. This suggests that, in the shell, the O partially substitutes the S and I. Noting that no Sb_2O_3 crystal phase was detected by the XRD, HRTEM, and HAADF-STEM, the shell should be an amorphous quaternary compound $SbO_xS_yI_{3-2x-2y}$. EDS mapping analysis shows $x \approx 1.14$ and $y \approx 0.22$ (Figure S10 and Tables S1 and S2).

The XPS survey spectrum of the SbSI samples indicates the composition of the Sb, S, and I (Figure 4a). Figure 4b shows that the peaks of Sb $3d_{5/2}$ and Sb $3d_{3/2}$ are located at 529.5 and 539.0 eV, respectively. There is a peak shoulder at around 531.0 eV, which can be fitted with a Gaussian function and attributed to the O 1s state. Compared with the Sb $3d_{5/2}$ peak, the intensity ratio of O 1s is weak for the freshly milled SbSI powder, while significantly enhanced for the size-selected samples that treated in water and dried in air. It is supported by the fact that the freshly milled SbSI NCs protected in toluene show a crystalline surface without an amorphous shell (Figure S11). The XPS peak accompanied by Sb $3d_{5/2}$ within 530−534 eV was also reported to result from the surface states dependent on temperature and specific crystalline surface.[52] This possibility can be ruled out for the SbSI studied here, since there are no such coexisted peaks for Sb $3d_{3/2}$, I $3d_{5/2}$, and I $3d_{3/2}$ (Figure 4c). All of the peaks of the Sb 3d, S 2p, I 3d, and valence bands are consistent with the reported values of SbSI.[53]

Photocatalytic Performance and Mechanisms of the SbSI NCs. The photocatalytic performance of the SbSI NCs was investigated for the degradation of MO, a typical pollutant

DOI: 10.1021/acssuschemeng.8b02498
ACS Sustainable Chem. Eng. 2018, 6, 12166−12175

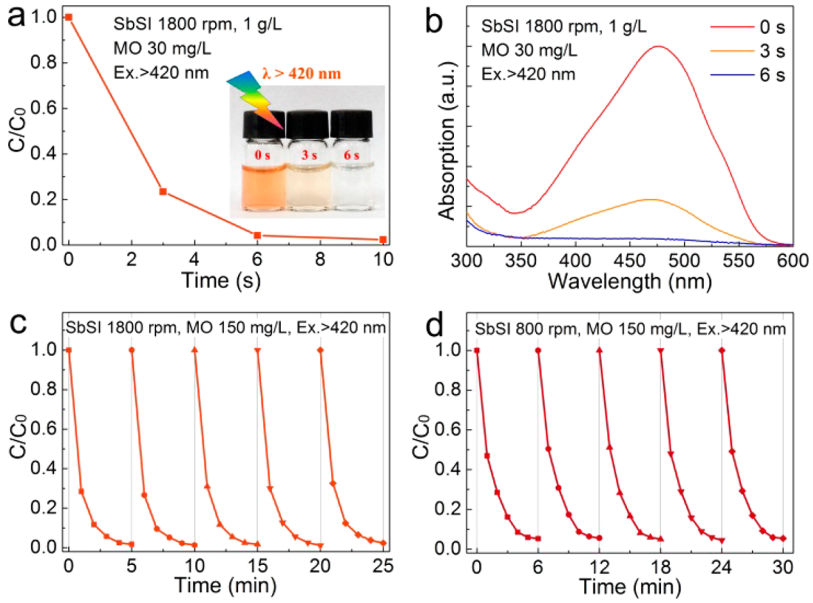

Figure 5. (a) The visible light photodegradation profile with the MO concentration of 30 mg/L for SbSI NCs 1800 rpm, and (b) the corresponding absorption spectrum. The visible light photodegradation cycles of MO at concentration of 150 mg/L for SbSI NCs of (c) 1800 and (d) 800 rpm fractions, at room temperature.

Table 1. Visible Light Photodegradation Efficiencies of MO by Various Photocatalysts[a]

ref	photocatalyst	dye: MO	photodegradation efficiency	light source, filter
54	P-,S-g−C_3N_4: 50 mg	10 mg/L, 100 mL	60 min, 73%, k = 0.021 min^{-1}	300 W XL, $\lambda \geq 420$ nm
55	g-C_3N_4−ZnO: 300 mg	4 mg/L, 100 mL	80 min, 97%	500 W XL, $\lambda > 420$ nm
56	Sb_2S_3/g−C3N4: 100 mg	10 mg/L, 100 mL	60 min, 80%	350 W XL, $\lambda \geq 420$ nm
57	Sb_2S_3: 40 mg	20 mg/L, 80 mL	30 min, 97%	500 W HL, 420 < λ < 800 nm
58	CdS-C: 25 mg	5 mg/L, 100 mL	40 min, 96.6%	500 W XL, $\lambda \geq 420$ nm
59	$SnIn_4S_8$: 15 mg	10 mg/L, 80 mL	210 min, ∼100%	300 W HL, 400 < λ < 800
21	BiOBr: 400 mg	10 mg/L, 400 mL	300 min, ∼100%	300 W XL, $\lambda \geq 420$ nm
60	ZnO/BiOI: 100 mg	10 mg/L, 100 mL	240 min, 78%	500 W HL, $\lambda \geq 420$ nm
61	AgBr/GA: 24 mg	10 mg/L, 10 mL	8 min, ∼100%, k = 0.72 min^{-1}	500 W XL, $\lambda \geq 420$ nm
62	Ag/AgCl/$SrTiO_3$: 50 mg	10 mg/L, 100 mL	40 min, 93%	300 W XL, $\lambda \geq 420$ nm
63	Ag_2O/Ag_2CO_3: 50 mg	20 mg/L, 100 mL	5 min, ∼100%, k = 0.92 min^{-1}	150 W HL, 400 <λ < 660 nm
64	Ag_2O: 30 mg	16 mg/L, 10 mL	2 min, ∼90%	500 W XL, $\lambda \geq 380$ nm
65	Ag/Ag_2O: 100 mg	20 mg/L, 100 mL	10 min, ∼90%	300 W XL, $\lambda \geq 420$ nm
66	Ag_2S−Ag: 8 mg	5 mg/L, 20 mL	30 min, 92.1%	500 W XL, $\lambda \geq 420$ nm
67	Ag_3PO_4: 200 mg	8 mg/L, 100 mL	4 min, ∼98%	500 W XL, $\lambda \geq 420$ nm
68	Pt-$CaCu_3Ti_4O_{12}$: 100 mg	20 mg/L, 50 mL	360 min, 80%	300 W XL, $\lambda \geq 420$ nm
69	CNTs/P-TiO_2: 100 mg	20 mg/L, 250 mL	240 min, ∼95%	400 W HL, $\lambda \geq 410$ nm
70	Bi_2WO_6/TiO_2: 20 mg	20 mg/L, 20 mL	40 min, ∼95%	300 W XL, UV filtered out
		20 mg/L, 20 mL	25 min, ∼97%	300 W ML, (356 nm)
71	WS_2: 50 mg	20 mg/L, 50 mL	300 min, ∼90%	350 W XL, $\lambda \geq 420$ nm
		20 mg/L, 50 mL	100 min, ∼96%	300 W ML, (356 nm)
34	black phosphorus: 5 mg	6 mg/L, 100 mL	20 min, 90%	300 W XL, $\lambda \geq 600$ nm
13	TiO_2(B):C: 50 mg	7 mg/L, 102 mL	40 min, ∼84%	300 W XL, $\lambda \geq 420$ nm
	TiO_2(B):I: 50 mg	7 mg/L, 102 mL	50 min, ∼62%	300 W XL, $\lambda \geq 420$ nm
this work	SbSI NCs 1800 rpm: 50 mg	30 mg/L, 50 mL	10 s, ∼99%, k = 0.42 s^{-1}, RT	300 W XL $\lambda \geq 420$ nm
	SbSI NCs 1800 rpm: 50 mg	150 mg/L, 50 mL	5 min, ∼98%, k = 0.014 s^{-1}, RT	300 W XL $\lambda \geq 420$ nm
	SbSI NCs 1800 rpm: 50 mg	150 mg/L, 50 mL	30 s, ∼99%, k = 0.15 s^{-1}, at 65°	300 W XL $\lambda \geq 420$ nm
	SbSI NCs 1800 rpm: 200 mg	150 mg/L, 50 mL	1 min, ∼99%, k = 0.095 s^{-1}, RT	300 W XL $\lambda \geq 420$ nm

[a]Note: XL: Xe lamp; HL: halogen lamp; ML: mercury lamp; and RT: room temperature (∼20 °C).

of anionic azo dye resulting from the textile industry. Figure 5a,b shows the room temperature photodegradation of 30 mg/L MO under a 300 W Xe lamp and a 420 nm cut-off filter by using the SbSI NCs of the 1800 rpm fraction. The sampling shows 96% of the MO was degraded in 6 s, and 99% degraded in 10 s. The MO concentration after the adsorption equilibrium was used as the initial concentration (C_0). By a linear fitting of $\ln(C_0/C)$ to time, the pseudo-first-order rate constant (k) of the photodegradation was calculated to be 0.42 s^{-1}. With other parameters unchanged, a 98% degradation was

DOI: 10.1021/acssuschemeng.8b02498
ACS Sustainable Chem. Eng. 2018, 6, 12166−12175

achieved in 5 min (k = 0.014 s^{-1}) for the MO solution with a high concentration up to 150 mg/L. Table 1 summarizes reported typical results of the visible light photodegradation efficiencies of MO by various photocatalysts. The SbSI NCs in this report achieve an outstanding record performance as far to date.

Cycling Performance. The photocatalytic cycling property of the SbSI is fairly good (Figure 5c,d). The HRTEM and XRD measurements indicate that the structure of the SbSI NCs remains after the photodegradation cycling (Figures S9 and S12). The EDS (equipped in SEM) measurements show that the component of the samples is almost unchanged, with an Sb:S:I ratio of about 1:0.83:0.83 (Figure S13). However, the XPS analysis suggests the loss of I, from the Sb:S:I ratio of 1:0.75:0.54 to 1:0.75:0.41 before and after the photodegradation cycling, respectively (Figure S14). At the same time, the states of Sb 3d, I 3d, and S 2p present no noticeable change. The lower ratio of I measured by XPS may due to the limited detection depth of XPS compared with that of the EDS, consistent with the EDS mapping results. It means that the possible oxidization occurs on the surface layer with the loss of I, which does not change the material structure and chemical state, thus having little effect on the photocatalytic performance.

Size Effect. The photocatalytic rate constant basically increases as the SbSI fractions changes from 500 to 1800 rpm fractions (Figure 6). In extreme cases, the photocatalytic

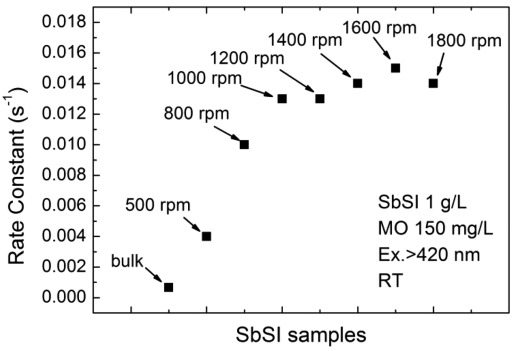

Figure 6. Photocatalytic rate constant of various SbSI samples for MO.

performance of the bulk SbSI crystal before milling is much lower. Two typical fractions of the 800 and 1800 rpm samples were investigated intensively for comparison. Although the SbSI NCs of lower rpm values are more effective in absorbing light at a longer wavelength (Figure 1c), are visibly light active, and cycle well, the SbSI NCs of higher rpm values have a better photocatalytic performance. This may due to the size effect of the SbSI samples. First, the exciton energy of the smaller SbSI is higher, and the bandgap is wider. Second, a higher specific surface of the SbSI has a more effective adsorption and degradation of MO. The BET analysis of the N_2 adsorption–desorption isotherms (Figure 7) shows that the BET specific area of the SbSI NCs 800 rpm is 4.06 m^2/g and for the SbSI NCs 1800 rpm is 10.67 m^2/g. The SbSI adsorption of MO in solution was carried out in the dark with stirring. The spectral measurements show that the adsorption equilibrium of MO was established within 20 min. For 150 mg/L MO, the adsorptions of SbSI NCs 800 and 1800 rpm are 12.7 and 16.3%, respectively; for 30 mg/L MO, the adsorptions of SbSI

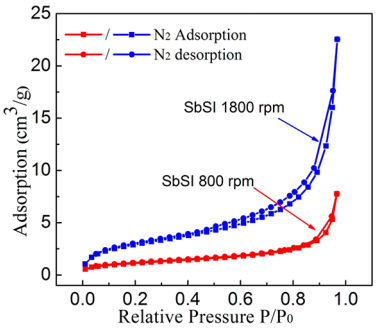

Figure 7. N_2 adsorption isotherms of SbSI NCs measured at 77 K.

NCs 800 and 1800 rpm are 17.5 and 19.4%, respectively. Therefore, the decolorization of the MO solution is due to photodegradation rather than adsorption. A short video of a control experiment to compare the photodegradation and adsorption are shown in the Supporting Information.

The transient photocurrent responses of the SbSI NCs 800 and 1800 rpm are shown in Figure 8. The photocurrent–time

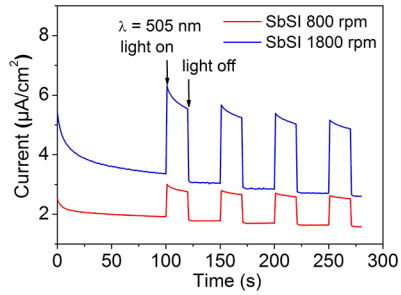

Figure 8. Transient photocurrent responses of the SbSI NCs with the excitation wavelength of 505 nm.

(I–t) curves were measured with typical on–off cycles with an intermittent visible light irradiation wavelength of 505 nm. The experiments were carried out in a 0.1 M Tris-HCl buffer saline (pH 7.4) containing 0.05 M potassium chloride and 0.1 M sodium chloride. The working ITO electrode was modified by the SbSI NCs of the same loading amount. It shows that the photocurrent value of the SbSI NCs 1800 rpm is significantly higher than that of the 800 rpm fraction, indicating the higher carrier generation efficiency of the former. A similar transient photocurrent response at 430 nm is given in Figure S15.

Role of Singlet Oxygen. Under the illumination, the SbSI NCs produce excitons composed of electron (e^-) and hole (h^+) pairs, which will induce the reactive oxygen species (ROS), such as superoxide radicals ($^{\bullet}O_2^-$), hydroxyl radicals ($^{\bullet}OH$), hydrogen peroxide (H_2O_2), and singlet oxygen ($^1O_2$). Various scavenging/trapping agents were used to elucidate the mechanism of the efficient MO degradation: superoxide dismutase (SOD) for $^{\bullet}O_2^-$, isopropanol for $^{\bullet}OH$, catalase for H_2O_2, carotene, and sodium azide (NaN_3) for singlet oxygen. Figure 9a suggests that all of these ROS exist for the visible light degradation. By adding scavenging/trapping agents of SOD, isopropanol, and catalase, the photodegradation efficiency in 5 min decreases from 98 to 82, 78, and 81%, respectively, indicating that $^{\bullet}O_2^-$, $^{\bullet}OH$, and H_2O_2 have minor contributions. While by adding carotene or sodium azide, the photodegradation efficiency in 5 min drastically decreased to 27 or 21%, respectively. Therefore, $^1O_2$ is the dominant factor for the MO photodegradation. $^1O_2$ was also detected by a

DOI: 10.1021/acssuschemeng.8b02498
ACS Sustainable Chem. Eng. 2018, 6, 12166–12175

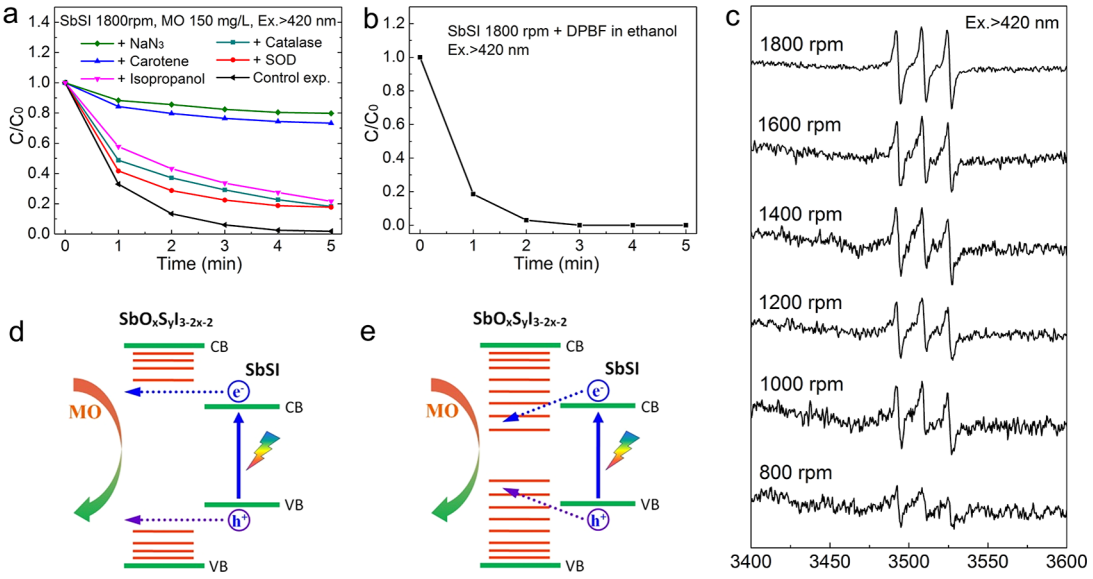

Figure 9. Visible light photodegradation profiles of (a) MO in the presence of scavenging/trapping agents of NaN_3, carotene, isopropanol, catalase, and SOD, and (b) DPBF in ethanol. (c) The EPR spectra of SbSI NCs in the presence of TEMP and >420 nm visible light irradiation. Schematic illustration of the charge transfer mechanisms: (d) the charge carrier tunneling and (e) the defect state-facilitated charge carrier transfer.

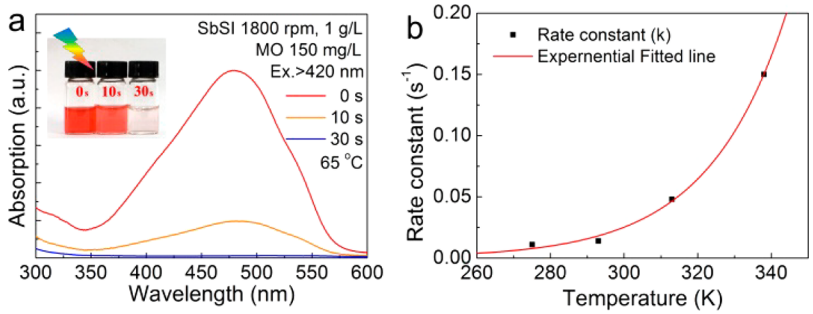

Figure 10. (a) The visible light photodegradation profile of MO with concentration of 150 mg/L at 65 °C. (b) The photodegradation rate constant to temperature curve.

widely used method, the bleaching of 1,3-diphenylisobenzofuran (DPBF), characterized by the absorption decrease at 410 nm (Figure 9b). The existence of $^1O_2$ was further confirmed by the EPR characterization. The 2,2,6,6-tetramethylpiperidine (TEMP) was employed as the $^1O_2$ trapping agent in SbSI NC solution under visible light irradiation (>420 nm). $^1O_2$ was trapped by TEMP to form 2,2,6,6-tetramethylpiperidine-*N*-oxyl (TEMPO), which shows clear 1:1:1 triplet EPR signals (Figure 9c). The SbSI NC 800 rpm has the lowest signal intensity among the samples (SbSI 500 rpm precipitated during measurement and no EPR signal was obtained), consistent with the size effect.

Nanocrystal Structure. From the view of the core/shell energy structure, some possible mechanisms for the high photocatalytic performance of these SbSI NCs may relate to the $SbO_xS_yI_{3-2x-2y}$ ($x \approx 1.14$, $y \approx 0.22$) shell. Since the atom ratio of O is dominantly higher than S and I in the shell, it could be regarded as the S- and I-doped amorphous Sb_2O_3. The amorphous Sb_2O_3 has a wide bandgap of ~3.8 eV.[72] Therefore, it is likely to have the type-I structure; the Sb_2O_3 valence band is lower and the conduction band is higher than that of the SbSI. Theoretically, the type-I structured materials should not be a better photocatalyst than bare SbSI NCs, because the shell with a wide bandgap confines the exciton in the core and acts as a physical barrier that hinders the access of photo-generated charges to the surface and solvent. In this condition, the charge carriers would reach the shell surface by the tunneling mechanism (Figure 9d). Meanwhile, the shell may also passivate the SbSI surface trap states, leading to a longer lifetime of photon excited electron−hole pairs. This could be favorable for the photocatalysis. A similar passivation function has been demonstrated for various type-I core/shell NCs as a better photocatalyst than the core material, e.g., CdSe/CdS and CdS/ZnS.[73−76] Another possible mechanism is associated with the intrinsic feature of the S and I doping in the amorphous shell, which may induce additional defect states located within the amorphous Sb_2O_3 bandgap. When part of these interband states lies between the bandgap of the SbSI core, the charge carriers may transfer to the shell surface by this pathway (Figure 9e). In the case that the interband states match the electron or hole transfer solely, the type-II structure is formed. It would lead to efficient charge separation between the core and shell, which will promote the photocatalytic performance. Both the charge tunneling and defect states facilitated charge carrier transfer mechanisms, together with the energy transfer mechanism, they could be responsible for the generation of $^1O_2$.[77,78] It should be mentioned that the surface of the SbSI NCs is relatively clean, since no organic chemical is introduced during the milling and size selective

DOI: 10.1021/acssuschemeng.8b02498
ACS Sustainable Chem. Eng. 2018, 6, 12166−12175

centrifugation. The free organic ligands offer more adsorption sites for the dye and oxygen.

Temperature. Known as a ferroelectric, SbSI has a Curie point at around 22 °C, with the ferroelectric axis as the *c*-axis. It would be interesting to figure out how the photodegradation of the dye affected the spontaneous polarization of SbSI NCs below and above the Curie temperature. To assume that the intrinsic electric dipoles will interact with the photon-excited electron−hole pairs to separate them, a longer lifetime could be possible for a temperature lower than the Curie point, thus promoting the photocatalysis. The visible light degradation of MO (150 mg/L) by SbSI NCs 1800 rpm shows that, at lower temperature of 2−6 °C, it takes 5 min to reach an ∼94% degradation (k = 0.011 s^{-1}); at ∼20 °C, it results in ∼98% degradation in 5 min (k = 0.014 s^{-1}); and at higher temperatures of ∼65 °C, it takes only 30 s to get ∼99% degradation (k = 0.15 s^{-1}). The rate constant to temperature is well fitted to the first-order exponential function, as shown in Figure 10. It suggests that the spontaneous polarization is not a major factor for the photodegradation. The temperature (T) dependent rate constant (k) can be explained by the activation energy in an Arrhenius equation:

$$k = Ae^{-E_a/RT} \quad (1)$$

where A is the pre-exponential constant, E_a is the activation energy for the reaction, and R is the gas constant. By fitting the $k-T$ data, E_a is deduced to be 40.1 kJ/mol, a typical value compared with photodegradation of azo dyes of 20−80 kJ/mol.[79−81]

Concentration and Light Wavelength. Besides the temperature, the photodegradation rate constant depends on the concentration of SbSI NCs. By using a higher SbSI NC concentration, the visible light photodegradation of MO can be even faster and vice versa (Figure S17). With the SbSI NC concentration of 4 g/L, the 150 mg/L MO can be ∼99% degraded in 1 min at room temperature. Experiments also revealed that the good photocatalytic performance of the SbSI NCs extends to the UV spectrum. Under the UV light or full spectrum light, the SbSI NCs exhibit distinctly higher photodegradation of MO than that of the TiO_2 (P25) NCs (Figures S18 and S19). However, the SbSI NCs show no obvious photocatalytisis for MO under a 6 W NIR LED lamp of 850 nm.

CONCLUSIONS

In summary, a strategy of ball-milling followed by size selective centrifugation was developed to prepare SbSI NCs. These SbSI NCs show an UV−visible photo activity, especially a surprisingly high visible light efficiency for photocatalytic degradation of MO. The nano structure, size, and temperature together with the efficient generation of singlet oxygen are important factors for the outstanding visible light photocatalytic performance. The elemental resource abundance, good cycling performance, and simple and low cost of the ball-milling process are conductive for its industrial applications. In addition to be used as a catalyst for pollutant water treatment, application potentials of the SbSI NCs in light-assisted air cleaning, catalytic synthesis, and photodynamic therapy are also expected due its effective generation of singlet oxygen.

ASSOCIATED CONTENT

Supporting Information

The Supporting Information is available free of charge on the ACS Publications website at DOI: 10.1021/acssuschemeng.8b02498.

SEM, HRTEM, HAADF-STEM, EDS, and XPS analysis of the size, component, and structure of SbSI NCs; PEC response and CV curves; and photocatalytic characterization of the bulk SbSI, SbSI NCs, and TiO_2 nanocrystals (PDF)

A short video on the visible light degradation of MO with the SbSI NCs before size selection as the photocatalyst (AVI)

AUTHOR INFORMATION

Corresponding Authors

*E-mail: xuxx@njnu.edu.cn.
*E-mail: huijunfeng@126.com.
*E-mail: wangpeng@nju.edu.cn.

ORCID

Xiangxing Xu: 0000-0001-9135-9403
Yaqian Lan: 0000-0002-2140-7980
Xinping Wang: 0000-0002-1555-890X
Zhihui Dai: 0000-0001-7049-7217
Peng Wang: 0000-0002-3418-8035

Author Contributions

#C.W. and M.Z. contributed equally to this work.

Notes

The authors declare no competing financial interest.

ACKNOWLEDGMENTS

We acknowledge Prof. X. Wang for the valuable discussion. This work was supported by the National Natural Science Foundation of China (NSFC) (51572120, 21533012, and 21625502), Six Talent Peaks Project in Jiangsu Province (184080H102231), and Nanjing Normal University Young Leading Talent Fund (184080H20210).

REFERENCES

(1) Fujishima, A.; Honda, K. Electrochemical photolysis of water at a semiconductor electrode. *Nature* **1972**, *238*, 37−38.

(2) Lewis, N. S.; Rosenbluth, M. L. *Photocatalysis: Fundamentals and Applications*; Serpone, N., Pelizzetti, E., Eds.; Wiley-Interscience: New York, 1989.

(3) Hoffmann, M. R.; Martin, S. T.; Choi, W. Y.; Bahnemann, D. W. Environmental applications of semiconductor photocatalysis. *Chem. Rev.* **1995**, *95*, 69−96.

(4) Kubacka, A.; Fernández-García, M.; Colón, G. Advanced nanoarchitectures for solar photocatalytic applications. *Chem. Rev.* **2012**, *112*, 1555−1614.

(5) Linsebigler, A. L.; Lu, G. Q.; Yates, J. T. Photocatalysis on TiO_2surfaces: principles, mechanisms, and selected results. *Chem. Rev.* **1995**, *95*, 735−758.

(6) Konstantinou, I. K.; Albanis, T. A. TiO_2-assisted photocatalytic degradation of azo dyes in aqueous solution: kinetic and mechanistic investigations: A review. *Appl. Catal., B* **2004**, *49*, 1−14.

(7) Iskandar, F.; Nandiyanto, A. B.D.; Yun, K. M.; Hogan, C. J.; Okuyama, K.; Biswas, P. Enhanced photocatalytic performance of brookite TiO_2macroporous particles prepared by spray drying with colloidal templating. *Adv. Mater.* **2007**, *19*, 1408−1412.

(8) Akpan, U. G.; Hameed, B. H. Parameters affecting the photocatalytic degradation of dyes using TiO_2-based photocatalysts: A review. *J. Hazard. Mater.* **2009**, *170*, 520−529.

DOI: 10.1021/acssuschemeng.8b02498
ACS Sustainable Chem. Eng. 2018, 6, 12166−12175

(9) Petrella, A.; Petrella, M.; Boghetich, G.; Mastrorilli, P.; Petruzzelli, V.; Ranieri, E.; Petruzzelli, D. Laboratory scale unit for photocatalytic removal of organic micropollutants from water and wastewater. methyl orange degradation. *Ind. Eng. Chem. Res.* **2013**, *52*, 2201−2208.
(10) Dong, S.; Feng, J.; Fan, M.; Pi, Y.; Hu, L.; Han, X.; Liu, M.; Sun, J.; Sun, J. Recent developments in heterogeneous photocatalytic water treatment using visible light-responsive photocatalysts: a review. *RSC Adv.* **2015**, *5*, 14610−14630.
(11) Pelaez, M.; Nolan, N. T.; Pillai, S. C.; Seery, M. K.; Falaras, P.; Kontos, A. G.; Dunlop, P. S.M.; Hamilton, J. W.J.; Byrne, J. A.; O'Shea, K.; Entezari, M. H.; Dionysiou, D. D. A review on the visible light active titanium dioxide photocatalysts for environmental applications. *Appl. Catal., B* **2012**, *125*, 331−349.
(12) Bora, L. V.; Mewada, R. K. Visible/solar light active photocatalysts for organic effluent treatment: Fundamentals, mechanisms and parametric review. *Renewable Sustainable Energy Rev.* **2017**, *76*, 1393−1421.
(13) Xiang, G.; Li, T.; Zhuang, J.; Wang, X. Large-scale synthesis of metastable TiO_2(B) nanosheets with atomic thickness and their photocatalytic properties. *Chem. Commun.* **2010**, *46*, 6801−6803.
(14) Asahi, R.; Morikawa, T.; Ohwaki, T.; Aoki, K.; Taga, Y. Visible-light photocatalysis in nitrogen-doped titanium oxides. *Science* **2001**, *293*, 269−271.
(15) Sakthivel, S.; Kisch, H. Daylight photocatalysis by carbon-modified titanium dioxide. *Angew. Chem., Int. Ed.* **2003**, *42*, 4908−4911.
(16) Linic, S.; Christopher, P.; Ingram, D. B. Plasmonic-metal nanostructures for efficient conversion of solar to chemical energy. *Nat. Mater.* **2011**, *10*, 911−921.
(17) Chen, X.; Zhu, H. Y.; Zhao, J. C.; Zheng, Z. T.; Gao, X. P. Visible-light-driven oxidation of organic contaminants in air with gold nanoparticle catalysts on oxide supports. *Angew. Chem., Int. Ed.* **2008**, *47*, 5353−5356.
(18) He, R. A.; Cao, S. W.; Zhou, P.; Yu, J. G. Recent advances in visible light Bi-based photocatalysts. *Chin. J. Catal.* **2014**, *35*, 989−1007.
(19) Kudo, A.; Omori, K.; Kato, H. A novel aqueous process for preparation of crystal form-controlled and highly crystalline $BiVO_4$powder from layered vanadates at room temperature and its photocatalytic and photophysical properties. *J. Am. Chem. Soc.* **1999**, *121*, 11459−11467.
(20) Tian, G.; Chen, Y.; Zhou, W.; Pan, K.; Dong, Y.; Tian, C.; Fu, H. Facile solvothermal synthesis of hierarchical flower-like Bi_2MoO_6hollow spheres as high performance visible-light driven photocatalysts. *J. Mater. Chem.* **2011**, *21*, 887−892.
(21) Zhang, J.; Shi, F.; Lin, J.; Chen, D.; Gao, J.; Huang, Z.; Ding, X.; Tang, C. Self-assembled 3-D architectures of BiOBr as a visible light-driven photocatalyst. *Chem. Mater.* **2008**, *20*, 2937−2941.
(22) Li, Y.; Wang, J.; Yao, H.; Dang, L.; Li, Z. Efficient decomposition of organic compounds and reaction mechanism with BiOI photocatalyst under visible light irradiation. *J. Mol. Catal. A: Chem.* **2011**, *334*, 116−122.
(23) Zhao, H.; Zhang, Y.; Li, G.; Tian, F.; Tang, H.; Chen, R. Rhodamine B-sensitized BiOCl hierarchical nanostructure for methyl orange photodegradation. *RSC Adv.* **2016**, *6*, 7772−7779.
(24) Wang, X.; Maeda, K.; Thomas, A.; Takanabe, K.; Xin, G.; Carlsson, J. M.; Domen, K.; Antonietti, M. A metal-free polymeric photocatalyst for hydrogen production from water under visible light. *Nat. Mater.* **2009**, *8*, 76−80.
(25) Liang, Q.; Li, Z.; Bai, Y.; Huang, Z. H.; Kang, F.; Yang, Q. H. Reduced-sized monolayer carbon nitride nanosheets for highly improved photoresponse for cell imaging and photocatalysis. *Sci. China Mater.* **2017**, *60*, 109−118.
(26) Ge, J.; Lan, M.; Liu, W.; Jia, Q.; Guo, L.; Zhou, B.; Meng, X.; Niu, G.; Wang, P. Graphene quantum dots as efficient, metal-free, visible -light-active photocatalysts. *Sci. China Mater.* **2016**, *59*, 12−19.
(27) Liu, D.; Wang, J.; Bai, X.; Zong, R.; Zhu, Y. Self-assembled PDINH supramolecular system for photocatalysis under visible light. *Adv. Mater.* **2016**, *28*, 7284−7290.
(28) Zhang, L.; Huang, X.-H.; Hu, J. S.; Song, J.; Kim, I. A Hypercross-linked polynaphthalene semiconductor with excellent visible-light photocatalytic performance in the degradation of organic dyes. *Langmuir* **2017**, *33*, 1867−1871.
(29) Liu, W.; Liu, Z.; Wang, G.; Sun, X.; Li, Y.; Liu, J. Carbon coated Au/TiO_2mesoporous microspheres: a novel selective photocatalyst. *Sci. China Mater.* **2017**, *60*, 438−448.
(30) Xu, Z.; Zhuang, C.; Zou, Z.; Wang, J.; Xu, X.; Peng, T. Enhanced photocatalytic activity by the construction of a TiO_2/carbon nitride nanosheets heterostructure with high surface area via direct interfacial assembly. *Nano Res.* **2017**, *10*, 2193−2209.
(31) Tu, W.; Zhou, Y.; Zou, Z. Versatile graphene-promoting photocatalytic performance of semiconductors: basic principles, synthesis, solar energy conversion, and environmental applications. *Adv. Funct. Mater.* **2013**, *23*, 4996−5008.
(32) Upadhyay, R. K.; Soin, N.; Roy, S. S. Role of graphene/metal oxide composites as photocatalysts, adsorbents and disinfectants in water treatment: a review. *RSC Adv.* **2014**, *4*, 3823−3851.
(33) Cao, S.; Yu, J. g-C_3N_4-Based photocatalysts for hydrogen generation. *J. Phys. Chem. Lett.* **2014**, *5*, 2101−2107.
(34) Wang, H.; Yang, X.; Shao, W.; Chen, S.; Xie, J.; Zhang, X.; Wang, J.; Xie, Y. Ultrathin black phosphorus nanosheets for efficient singlet oxygen generation. *J. Am. Chem. Soc.* **2015**, *137*, 11376−11382.
(35) Wang, H.; Jiang, S.; Shao, W.; Zhang, X.; Chen, S.; Sun, X.; Zhang, Q.; Luo, Y.; Xie, Y. Optically switchable photocatalysis in ultrathin black phosphorus nanosheets. *J. Am. Chem. Soc.* **2018**, *140*, 3474−3480.
(36) Zhao, Y.; Eley, C.; Hu, J.; Foord, J. S.; Ye, L.; He, H.; Tsang, S. C. E. Shape-dependent acidity and photocatalytic activity of Nb_2O_5nanocrystals with an active TT (001) surface. *Angew. Chem., Int. Ed.* **2012**, *51*, 3846−3849.
(37) Zhang, J.; Xu, Q.; Feng, Z.; Li, M.; Li, C. Importance of the relationship between surface phases and photocatalytic activity of TiO_2. *Angew. Chem., Int. Ed.* **2008**, *47*, 1766−1769.
(38) Zhou, X.; Lan, J.; Liu, G.; Deng, K.; Yang, Y.; Nie, G.; Yu, J.; Zhi, L. Facet-mediated photodegradation of organic dye over hematite architectures by visible light. *Angew. Chem., Int. Ed.* **2012**, *51*, 178−182.
(39) Huang, W. C.; Lyu, L. M.; Yang, Y. C.; Huang, M. H. Synthesis of Cu_2O nanocrystals from cubic to rhombic dodecahedral structures and their comparative photocatalytic activity. *J. Am. Chem. Soc.* **2012**, *134*, 1261−1267.
(40) Nitsche, R.; Merz, W. J. Photoconduction in ternary V-VI-VII compounds. *J. Phys. Chem. Solids* **1960**, *13*, 154−155.
(41) Fatuzzo, E.; Harbeke, G.; Merz, W. J.; Nitsche, R.; Roetschi, H.; Ruppel, W. Ferroelectricity in SbSI. *Phys. Rev.* **1962**, *127*, 2036−2037.
(42) Kern, R. An electro-optical and electromechanical effect in SbSI. *J. Phys. Chem. Solids* **1962**, *23*, 249−253.
(43) Harbeke, G. Absorption edge in ferroelectric SbSI under electric fields. *J. Phys. Chem. Solids* **1963**, *24*, 957−963.
(44) Nowak, M.; Szperlich, P.; Bober, Ł; Szala, J.; Moskal, G.; Stróz, D. Sonochemical preparation of SbSI gel. *Ultrason. Sonochem.* **2008**, *15*, 709−716.
(45) Chen, G.; Li, W.; Yu, Y.; Yang, Q. Fast and low-temperature synthesis of one-dimensional (1D) single-crystalline SbSI microrod for high performance photodetector. *RSC Adv.* **2015**, *5*, 21859−21864.
(46) Nowak, M.; Nowrot, A.; Szperlich, P.; Jesionek, M.; Kepińska, M.; Starczewska, A.; Mistewicz, K.; Stróz, D.; Szala, J.; Rzychoń, T.; Talik, E.; Wrzalik, R. Fabrication and characterization of SbSI gel for humidity sensors. *Sens. Actuators, A* **2014**, *210*, 119−130.
(47) Varghese, J.; O'Regan, C.; Deepak, N.; Whatmore, R. W.; Holmes, J. D. Surface roughness assisted growth of vertically oriented ferroelectric SbSI nanorods. *Chem. Mater.* **2012**, *24*, 3279−3284.

DOI: 10.1021/acssuschemeng.8b02498
ACS Sustainable Chem. Eng. 2018, 6, 12166−12175

(48) Butler, K. T.; Frost, J. M.; Walsh, A. Ferroelectric materials for solar energy conversion: photoferroics revisited. *Energy Environ. Sci.* **2015**, *8*, 838−848.
(49) Godel, K. C.; Steiner, U. Thin film synthesis of SbSI microcrystals for self-powered photodetectors with rapid time response. *Nanoscale* **2016**, *8*, 15920−15925.
(50) Ye, H.; Yang, L.; Gu, P. Semiconducting ferroelectric SbSI quantum dots in amorphous matrix: preparation and optical properties. *Proc. SPIE* **2002**, *4918*, 99.
(51) Madelung, O. M. *Semiconductors: Data Handbook*, 3rd ed.; Springer: Berlin, 2004.
(52) Grigas, J.; Talik, E.; Lazauskas, V. X-ray photoelectron spectroscopy of ferroelectric semiconductor SbSI crystals. *Lith. J. Phys.* **2004**, *44*, 427−438.
(53) Nowak, M.; Talik, E.; Szperlich, P.; Stróz, D. XPS analysis of sonochemically prepared SbSI ethanogel. *Appl. Surf. Sci.* **2009**, *255*, 7689−7694.
(54) Jiang, L.; Yuan, X.; Zeng, G.; Chen, X.; Wu, Z.; Liang, J.; Zhang, J.; Wang, H.; Wang, H. Phosphorus- and sulfur-codoped g-C_3N_4facile preparation, mechanism insight, and application as efficient photocatalyst for tetracycline and methyl orange degradation under visible light irradiation. *ACS Sustainable Chem. Eng.* **2017**, *5*, 5831−5841.
(55) Sun, J. X.; Yuan, Y. P.; Qiu, L. G.; Jiang, X.; Xie, A. J.; Shen, Y. H.; Zhu, J. F. Fabrication of composite photocatalyst g-C_3N_4-ZnO and enhancement of photocatalytic activity under visible light. *Dalton Trans.* **2012**, *41*, 6756−6763.
(56) Wang, H.; Yuan, X.; Wang, H.; Chen, X.; Wu, Z.; Jiang, L.; Xiong, W.; Zeng, G. Facile synthesis of Sb_2S_3/ultrathin g-C_3N_4sheets heterostructures embedded with g-C_3N_4quantum dots with enhanced NIR-light photocatalytic performance. *Appl. Catal., B* **2016**, *193*, 36−46.
(57) Sun, M.; Li, D.; Li, W.; Chen, Y.; Chen, Z.; He, Y.; Fu, X. New photocatalyst, $Sb_2S_3$for degradation of methyl orange under visible-light irradiation. *J. Phys. Chem. C* **2008**, *112*, 18076−18081.
(58) Hu, Y.; Gao, X.; Yu, L.; Wang, Y.; Ning, J.; Xu, S.; Lou, X. W. Carbon-coated CdS petalous nanostructures with enhanced photostability and photocatalytic activity. *Angew. Chem., Int. Ed.* **2013**, *52*, 5636−5639.
(59) Yan, T.; Li, L.; Li, G.; Wang, Y.; Hu, W.; Guan, X. Porous $SnIn_4S_8$microspheres in a new polymorph that promotes dyes degradation under visible light irradiation. *J. Hazard. Mater.* **2011**, *186*, 272−279.
(60) Jiang, J.; Zhang, X.; Sun, P.; Zhang, L. ZnO/BiOI heterostructures: photoinduced charge-transfer property and enhanced visible-light photocatalytic activity. *J. Phys. Chem. C* **2011**, *115*, 20555−20564.
(61) Fan, Y.; Ma, W.; Han, D.; Gan, S.; Dong, X.; Niu, L. Convenient recycling of 3D AgX/graphene aerogels (X = Br, Cl) for efficient photocatalytic degradation of water pollutants. *Adv. Mater.* **2015**, *27*, 3767−3773.
(62) Yang, S. F.; Niu, C. G.; Huang, D. W.; Zhang, H.; Liang, C.; Zeng, G. M. $SrTiO_3$nanocubes decorated with Ag/AgCl nanoparticles as photocatalysts with enhanced visible-light photocatalytic activity towards the degradation of dyes, phenol and bisphenol A. *Environ. Sci.: Nano* **2017**, *4*, 585−595.
(63) Yu, C. L.; Li, G.; Kumar, S.; Yang, K.; Jin, R. C. Phase transformation synthesis of novel Ag_2O/Ag_2CO_3heterostructures with high visible light efficiency in photocatalytic degradation of pollutants. *Adv. Mater.* **2014**, *26*, 892−898.
(64) Jiang, W.; Wang, X. Y.; Wu, Z. M.; Yue, X. N.; Yuan, S. J.; Lu, H. F.; Liang, B. Silver oxide as superb and stable photocatalyst under visible and near-infrared light irradiation and its photocatalytic mechanism. *Ind. Eng. Chem. Res.* **2015**, *54*, 832−841.
(65) Wang, G.; Ma, X. C.; Huang, B. B.; Cheng, H. F.; Wang, Z. Y.; Zhan, J.; Qin, X. Y.; Zhang, X. Y.; Dai, Y. Controlled synthesis of Ag_2O microcrystals with facet-dependent photocatalytic activities. *J. Mater. Chem.* **2012**, *22*, 21189−21194.
(66) Yang, W.; Zhang, L.; Hu, Y.; Zhong, Y.; Wu, H. B.; Lou, X. W. Microwave-assisted synthesis of porous Ag_2S−Ag hybrid nanotubes with high visible-light photocatalytic activity. *Angew. Chem., Int. Ed.* **2012**, *51*, 11501−11504.
(67) Bi, Y.; Ouyang, S.; Umezawa, N.; Cao, J.; Ye, J. Facet effect of single-crystalline Ag_3PO_4sub-microcrystals on photocatalytic properties. *J. Am. Chem. Soc.* **2011**, *133*, 6490−6492.
(68) Clark, J. H.; Dyer, M. S.; Palgrave, R. G.; Ireland, C. P.; Darwent, J. R.; Claridge, J. B.; Rosseinsky, M. J. Visible light photooxidation of model pollutants using $CaCu_3Ti_4O_{12}$an experimental and theoretical study of optical properties, electronic structure, and selectivity. *J. Am. Chem. Soc.* **2011**, *133*, 1016−1032.
(69) Wang, S.; Zhou, S. Photodegradation of methyl orange by photocatalyst of CNTs/P-$TiO_{(2)}$under UV and visible-light irradiation. *J. Hazard. Mater.* **2011**, *185*, 77−85.
(70) Tian, J.; Sang, Y.; Yu, G.; Jiang, H.; Mu, X.; Liu, H. A Bi_2WO_6-based hybrid photocatalyst with broad spectrum photocatalytic properties under UV, visible, and near-infrared irradiation. *Adv. Mater.* **2013**, *25*, 5075−5080.
(71) Sang, Y.; Zhao, Z.; Zhao, M.; Hao, P.; Leng, Y.; Liu, H. From UV to near-infrared, WS_2nanosheet: a novel photocatalyst for full solar light spectrum photodegradation. *Adv. Mater.* **2015**, *27*, 363−369.
(72) Wood, C.; van Pelt, B.; Dwight, A. The optical properties of amorphous and crystalline Sb_2O_3. *Phys. Status Solidi B* **1972**, *54*, 701−706.
(73) Huang, L.; Wang, X.; Yang, J.; Liu, G.; Han, J.; Li, C. Dual cocatalysts loaded type I CdS/ZnS core/shell nanocrystals as effective and stable photocatalysts for H_2evolution. *J. Phys. Chem. C* **2013**, *117*, 11584−11591.
(74) Thibert, A.; Frame, F. A.; Busby, E.; Holmes, M. A.; Osterloh, F. E.; Larsen, D. S. Sequestering high-energy electrons to facilitate photocatalytic hydrogen generation in CdSe/CdS nanocrystals. *J. Phys. Chem. Lett.* **2011**, *2*, 2688−2694.
(75) Xie, Y. P.; Yu, Z. B.; Liu, G.; Ma, X. L.; Cheng, H.-M. CdS-mesoporous ZnS core-shell particles for efficient and stable photocatalytic hydrogen evolution under visible light. *Energy Environ. Sci.* **2014**, *7*, 1895−1901.
(76) Jiang, D.; Sun, Z.; Jia, H.; Lu, D.; Du, P. A cocatalyst-free CdS nanorod/ZnS nanoparticle composite for high-performance visible-light-driven hydrogen production from water. *J. Mater. Chem. A* **2016**, *4*, 675−683.
(77) Kanofsky, J. R.; Sugimoto, H.; Sawyer, D. T. Singlet Oxygen Production from the Reaction of Superoxide Ion with Halocarbons in Acetonitrile. *J. Am. Chem. Soc.* **1988**, *110*, 3698−3699.
(78) Duong, H. D.; Rhee, J. I. Singlet oxygen production by fluorescence resonance energy transfer (FRET) from green and orange CdSe/ZnS QDs to protoporphyrin IX (PpIX). *Chem. Phys. Lett.* **2011**, *501*, 496−501.
(79) Fan, J.; Guo, Y.; Wang, J.; Fan, M. Rapid decolorization of azo dye methyl orange in aqueous solution by nanoscale zerovalent iron particles. *J. Hazard. Mater.* **2009**, *166*, 904−910.
(80) Shih, Y. H.; Tso, C. P.; Tung, L. Y. Rapid degradation of methyl orange with nanoscale zerovalent iron particles. *J. Environ. Eng. Manage.* **2010**, *20*, 137−143.
(81) Xie, S. H.; Huang, P.; Kruzic, J. J.; Zeng, X. R.; Qian, H. X. A highly efficient degradation mechanism of methyl orange using Fe-based metallic glass powders. *Sci. Rep.* **2016**, *6*, 21947.

DOI: 10.1021/acssuschemeng.8b02498
ACS Sustainable Chem. Eng. 2018, 6, 12166−12175